Applied Catalysis B: Environmental 166–167 (2015) 445–453

Contents lists available at ScienceDirect

Applied Catalysis B: Environmental

journal homepage: www.elsevier.com/locate/apcatb

Noble-metal-free MoS_2 co-catalyst decorated UiO-66/CdS hybrids for efficient photocatalytic H_2 production

Lijuan Shen, Mingbu Luo, Yuhao Liu, Ruowen Liang, Fenfen Jing, Ling Wu*

State Key Laboratory of Photocatalysis on Energy and Environment, Fuzhou University, Fuzhou 350002, PR China

ARTICLE INFO

Article history:
Received 17 October 2014
Received in revised form
24 November 2014
Accepted 30 November 2014
Available online 3 December 2014

Keywords:
Photocatalytic H_2 evolution
MOFs
CdS
MoS_2
Noble-metal-free

ABSTRACT

A novel and highly efficient photocatalyst MoS_2/UiO-66/CdS has been fabricated through dual modification of CdS with metal-organic framework (MOF) UiO-66 and MoS_2. UiO-66 was firstly introduced as a matrix for the well-dispersed growth of CdS, resulting in large active surface area. Moreover, the heterojunction between UiO-66 and CdS promoted the separation of photogenerated electron–hole pairs. MoS_2 as cocatalyst was further deposited on UiO-66/CdS *via* a facile photo-assisted approach. This technique made CdS, UiO-66 and MoS_2 undergo an intimate interfacial interaction, setting a stage for rapid transfer of photogenerated electrons between the components of the composite, and hence dramatically increased the synergetic catalytic effect of UiO-66, MoS_2 and CdS. Without a noble-metal cocatalyst, the obtained MoS_2/UiO-66/CdS composites functioned as high-performance photocatalysts for H_2 evolution under visible light irradiation. An unusual H_2 production rate of 650 μmol h^{-1} has been reached by the sample of MoS_2/UiO-66/CdS when the content of UiO-66 is 50 wt% and MoS_2 is 1.5 wt%. This is nearly 60 times higher than the H_2 evolution rate with pure CdS and also exceeds that of Pt/UiO-66/CdS under the same reaction conditions. More importantly, in sharp contrast with the obvious deterioration in photoactivity of pure CdS, the MoS_2/UiO-66/CdS displayed significantly enhanced photostability. This study clearly demonstrates the benefit of using MOFs as ideal support and MoS_2 as cocatalyst to work cooperatively for enhancing the photocatalytic H_2 evolution activity and stability of semiconductors.

1. Introduction

The search for renewable energy alternatives to fossil fuels is an important yet challenging issue in this century [1]. Photocatalytic H_2 generation from water by using solar energy provides an alternative environmentally benign way, but the key is to develop highly active and stable photocatalysts at low cost [2–4]. So far, various photocatalysts have been developed for H_2 production, including oxide [5], sulfide [6], and nitride semiconductors [7]. Among the reported materials, CdS has received a special attention due to its narrow bandgap (around 2.4 eV) and the correct band alignment for water photolysis [8,9]. However, some important factors still hinder the practical application of pure CdS for H_2 production. For example, the CdS nanoparticles are apt to aggregate during the synthesis process, resulting in a reduced surface area and the masking effect of active sites [10]. High recombination of the photoinduced electron–hole pairs also competes with the photocatalytic H_2 production reaction and lowers the solar energy conversion efficiency of CdS [11]. In addition, photocorrosion problem is widely considered to be a major weakness of CdS that could negate its potential advantages from an applications perspective [12]. To solve these problems, many approaches have been proposed, such as synthesis of quantum-sized CdS [13], coupling CdS with other semiconductors and cocatalysts [14–19], or incorporation of CdS into porous materials that possess large specific surface area [20,21].

Emerging as a new class of porous material, metal-organic frameworks (MOFs) have attracted tremendous attention owing to their exciting characteristics, such as high surface areas, crystalline open structures, tunable pore size, and functionality [22–26]. Some recent publications have highlighted the superiority of using MOFs as support for semiconductor due to that (i) MOFs as matrix can control the size of semiconductor particles; (ii) the high specific surface area of MOFs may create more catalytic sites and make better contact between reactants and active sites; and (iii) the host porous structures of MOFs can also provide extra pathways for the migration of photoinduced electrons and thus facilitate the charge carriers separation [27–29]. For all these reasons, MOFs could be a judicious choice to couple with CdS. More importantly, it has been reported that some photoactive MOFs like MOF-5 [30], UiO-66-NH_2 [31], MIL-100(Fe) [32], and NH_2-MIL-125(Ti) behavior as

* Corresponding author. Tel.: +86 591 83779362; fax: +86 591 83779105.
E-mail address: wuling@fzu.edu.cn (L. Wu).

http://dx.doi.org/10.1016/j.apcatb.2014.11.056
0926-3373/

semiconductor [33,34]. Consequently, it could be inferred that a photoactive MOF can not only serve as a host to control the growth of CdS, but also facilitate the separation of photogenerated charge carriers by forming the effective heterostructure with CdS when the two components have well-matched band structures.

On the other hand, the cocatalyst loaded on semiconductor photocatalyst plays an essential role in the production of H_2 [35,36]. Pt is known to catalyze the H_2 evolution reaction very efficiently, however, the widespread use of Pt is limited by its scarcity and high cost [37,38]. Against this background, recently, molybdenum disulfide (MoS_2), with a structure composed of three stacked atom layers (S—Mo—S) held together by van der Waals forces, has been widely investigated and considered to be a promising alternative to Pt as an efficient cocatalyst for H_2 evolution due to its high abundance and low cost [39–41]. Thereby, it can be expected that the further introduction of MoS_2 into the MOF–CdS system may achieve noble-metal-free photocatalysts with high catalytic activities. Unfortunately, to date, the dual modification of CdS with MOFs and MoS_2 cocatalyst aiming at a synergetic combination of their intrinsic outstanding properties to enhance the photocatalytic H_2 evolution of CdS is still scarce in the literature. Additionally, despite the recent progress on the synthesis and application of MoS_2 cocatalyst for enhancing the photoactivity of CdS, the reported MoS_2/CdS-based photocatalysts still suffer from one or more of the following drawbacks: (i) the synthetic procedures for the preparation of MoS_2 often need harsh reaction conditions (*e.g.* high-temperature and long-time solvothermal treatment, strictly tuning the pH of the reaction solution, reduction by toxic H_2S streams and annealing at high temperature), which greatly hinder the practical implementation of MoS_2 cocatalyst [42–44]; (ii) large surface area of the photocatalysts can boost reactant adsorbability giving high reaction possibility, however, the reported MoS_2/CdS-based photocatalysts generally possess low surface area and the prepared CdS shows different degree of aggregation [44,45]; (iii) the photocatalytic H_2 activities of some CdS-based photocatalysts are still unsatisfactory even in the presence of MoS_2 cocatalyst and sacrificial agent [41,45]. Therefore, it is highly desirable to prepare MoS_2 modified CdS-based photocatalyst with large surface area and less aggregation by a facile and easily accessible way for efficient H_2 evolution from water.

Toward this end, herein, we report for the first time by using MOF and MoS_2 to modify the CdS for use in photocatalytic H_2 production. UiO-66, as a typical MOF constituted by zirconium-oxo clusters and terephthalates, is chosen to integrate with CdS due to its porosity, unprecedented stability and semiconductor property [46]. UiO-66/CdS was first prepared *via* a facile one-step hydrothermal method, and then MoS_2 was deposited on UiO-66/CdS by the room-temperature photodeposition approach. It has been found that the introduction of UiO-66 efficiently hinders the aggregation of CdS during the synthesis process, forming UiO-66/CdS composites with large surface area. Moreover, the synergic action of UiO-66 and MoS_2 leads to efficient separation of the photogenerated charge carriers and simultaneously provides a large number of active reactive sites, consequently, enhance the photocatalytic H_2 production activity and stability of the MoS_2/UiO-66/CdS composite. It is hoped that the current work could inspire growing interest on the fabrication of other high-performance MOFs/MoS_2/semiconductor composite by taking the advantage of MOFs and MoS_2.

2. Experiment section

2.1. Preparation of photocatalysts

All chemicals were obtained commercially and used without further purification.

2.1.1. Synthesis of UiO-66

UiO-66 was synthesized by a modified solvothermal method based on a previous work [47]. In a typical synthesis, $ZrCl_4$ (0.2332 g, 1.0 mmol) and terephthalic acid (H_2BDC) (0.1661 g, 1.0 mmol) were dissolved in DMF (50 mL), then the solution was transferred into a 100 mL Teflon-lined stainless steel autoclave. The autoclave was sealed and heated in an oven at 120 °C for 24 h. After cooled naturally, the sample was purified with anhydrous methanol for several times to make sure that the occluded DMF molecules were eliminated, followed by drying under vacuum (100 °C, 12 h), the final UiO-66 sample was obtained.

2.1.2. Synthesis of Pure CdS

The procedure for the synthesis of CdS is similar to the previous report with a little modification [48]. 0.5 g of $Cd(CH_3COO)_2{\cdot}2H_2O$ was dispersed in 50 mL of dimethyl sulfoxide (DMSO). After vigorous stirring, the suspension was transferred into a 100 mL Teflon-lined autoclave and heated at 180 °C for 12 h. After that, the product was cooled to room temperature, and the precipitate was collected by centrifugation and then purified with acetone and ethanol several times to remove the residue of DMSO. The final product was dried at 60 °C under vacuum.

2.1.3. Synthesis of UiO-66/CdS

UiO-66/CdS composites were prepared using the same method as that for the preparation of pure CdS. The difference is the introduction of UiO-66 in the first step. A varying amount of UiO-66 and $Cd(CH_3COO)_2{\cdot}2H_2O$ were dispersed in 50 mL of DMSO. The suspension was transferred into a 100 mL Teflon-lined autoclave and heated at 180 °C for 12 h. After that, the products were cooled to room temperature, and the precipitates were collected by centrifugation and then purified with acetone and ethanol several times to remove the residue of DMSO. The final products were dried at 60 °C under vacuum. The obtained samples were labeled as (*X*) U6–CdS where *X* = 20, 30, 40, 50, 60 and 70% according the weight addition ratios of UiO-66 in the composites.

2.1.4. Synthesis of MoS_2/UiO-66/CdS

MoS_2 was synthesized according to the literature [49]. A 2.5×10^{-4} mol dm^{-3} $(NH_4)_2MoS_4$ solution (solvent = H_2O/C_2H_5OH = 15 mL/5 mL) was placed in a reaction vessel, and then the as-prepared (*X*) U6/CdS was dispersed into the mixed solution. After the solution had been bubbled with nitrogen for 0.5 h in the dark, irradiation was carried out with a 300 W Xe lamp (PLS-SXE 300, Beijing Perfectlight Co. Ltd.). After that, the precipitate was collected by centrifugation, washed with distilled water, and then dried in an oven at 60 °C. The obtained samples were labeled as MoS_2/U6–CdS.

2.2. Characterizations

Powder X-ray diffraction (XRD) patterns were obtained on a Bruker D8 Advance X-ray diffractometer operated at 40 kV and 40 mA with Ni-filtered Cu Kα irradiation (λ = 1.5406 Å). UV–vis diffuse reflectance spectra (UV–vis DRS) were obtained by a UV-vis spectrophotometer (Varian Cary 500) with barium sulfate as a referent. BET surface area and the N_2 adsorption were carried out on an ASAP2020M apparatus (Micromeritics Instrument Corp., USA). The samples were degassed in vacuum at 120 °C for 6 h and then analyzed at 77 K. Transmission electron microscopy (TEM) analysis was conducted on a JEM-2100F electron microscope (JEOL, Japan), using a 200 kV accelerating voltage. Scanning electron microscopy (SEM) analysis was performed using a S-4800 microscope (Hitachi, Japan). X-ray photoelectron spectroscopy (XPS) measurements were performed on a PHI Quantum 2000 XPS system with a monochromatic Al Kα source and a charge neutralizer. The concentration of the Cd

and Zr ions in solution was quantified by an inductively coupled plasma emission spectroscopy (ICP, Perkin Elmer Optima 2000DV). The photoluminescence spectra (PL) for solid samples were investigated on an Edinburgh FL/FS900 spectrophotometer.

2.3. Electrochemistry measurements

The working electrode was prepared on fluorine-doped tin oxide (FTO) glass, which was cleaned by sonication in deionized water and ethanol for 30 min, and then drying at 80 °C. The FTO slide was dip coated with 10 μL of slurry, which was obtained from the mixture of 5 mg photocatalyst and 0.5 mL H_2O under sonication for 2 h, and the side part of the FTO slide was previously protected using Scotch tape. After air drying naturally, a copper wire was connected to the side part of the FTO glass using a conductive tape. The uncoated parts of the electrode were isolated with an epoxy resin, and the exposed area of the electrode was 0.25 cm^2. The electrochemical measurements were performed in a conventional three electrode cell, using a Pt plate and a saturated Ag/AgCl electrode as counter electrode and reference electrode, respectively. The working electrodes were immersed in a 0.2 M Na_2SO_4 aqueous solution without any additive for 30 s before measurement. The photocurrent measurements were conducted with a BAS Epsilon workstation. A 300 W Xe lamp (PLS-SXE 300, Beijing Perfectlight Co. Ltd.) with a 420 nm cut-off filter was used as a light source.

2.4. Evaluation of photocatalytic activity

The photocatalytic H_2 production experiments were performed in a Pyrex reaction cell connected to a closed gas circulation and evacuation system. 20 mg of the prepared samples were suspended in 80 mL of aqueous solution containing 10% of lactic acid (LA) in volume as a sacrificial agent. The suspension was then thoroughly degassed and irradiated by a Xe lamp (300 W) (PLS-SXE 300, Beijing Perfectlight Co. Ltd.), which is equipped with an optical filter ($\lambda \geq 420$ nm) to cut off the light in the ultraviolet region. The amount of hydrogen evolved was determined at an interval of 1 h with online gas chromatography (Fuli, GC 7890, MS-5 A column, TCD, Ar carrier). The apparent quantum efficiency (AQE) of H_2 production was also measured under the same photocatalytic reaction conditions except that a 420 nm band-pass filter was used ($\lambda = 420 \pm 10$ nm). The number of incident photons was measured using a Si photodiode (ILT 950). The AQE was calculated according to the following equation [11]:

$$\mathrm{AQE}(\%) = \frac{\text{Number of reacted electrons}}{\text{Number of incident photons}} \times 100 = \frac{\text{Number of evolved } H_2 \text{ molecules} \times 2}{\text{Number of incident photons}} \times 100$$

3. Results and discussion

3.1. Characterizations

Fig. 1 shows the XRD patterns of pure UiO-66, CdS and U6–CdS composites with different weight contents of UiO-66. The diffraction peaks of the UiO-66 can be well matched with the previous report [46], demonstrating that UiO-66 has been successfully synthesized. The pure CdS shows the diffraction peaks which can be indexed to hawleyite CdS phase (JCPDS No. 10-0454). The peaks at 2θ values of 26.5°, 43.9°, 52.1°, and 70.4° can be assigned to the (1 1 1), (2 2 0), (3 1 1), and (3 3 1) crystal planes of hawleyite CdS, respectively [48]. With small percentage of UiO-66 in the composite, the characteristic peaks of UiO-66 cannot be clearly identified in the XRD pattern. This might be due to the complete

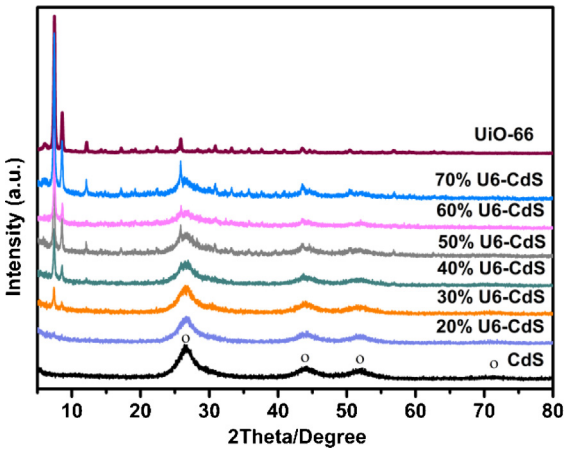

Fig. 1. XRD patterns of pure UiO-66, CdS and U6–CdS composites with different weight ratios of UiO-66.

occupation of CdS on the surface of UiO-66. However, when the content of UiO-66 is increased to 30% in the composite, the U6–CdS composite exhibits distinct diffraction peaks corresponding to UiO-66 and CdS, respectively, reflecting a two-phase composition of UiO-66 and CdS in these composites and further suggesting that the integrity of the UiO-66 framework is maintained after coupling with CdS.

UV–vis diffuse reflectance spectra (DRS) measurement has been performed to study the optical property of the samples. As shown in Fig. 2, the UiO-66 shows its fundamental absorption edge at about 320 nm. The pure CdS has absorption in the visible range with a band edge at 510 nm. All of the U6–CdS composites exhibit broader absorption in the visible light region. The light absorption of the U6–CdS composites in the range from 320 to 510 nm is positive correlation to the content of CdS, which is in agreement with the color change of the samples. In addition, it is notable that the position of adsorption edge of U6–CdS composites shows a blue shift as compared to pure CdS, which can be ascribed to the quantum confinement effect [50], implying that the introduction of UiO-66 as support can control the size of CdS.

The N_2 adsorption–desorption measurement has been carried out to study the specific surface area and porosity of the as-prepared samples. The isotherm of UiO-66 belongs to the typical type I, indicating the presence of the micropores as described in literature [51]. The pure CdS displays a type II isotherm, indicating nonporous or macroporous structure (Fig. S1, Supplementary

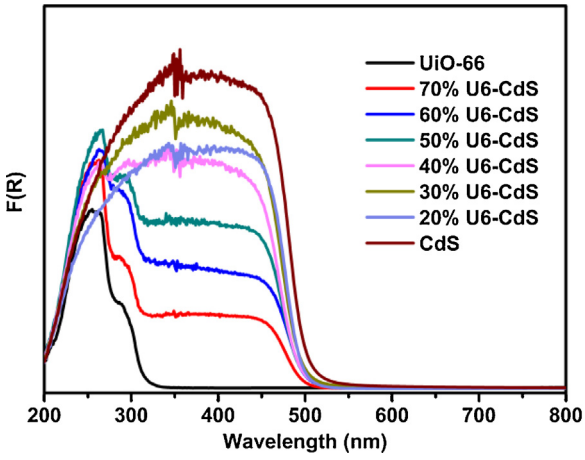

Fig. 2. UV–vis diffuse reflectance spectra of the pure UiO-66, CdS and U6–CdS composites with different weight ratios of UiO-66.

Table 1
BET surface area, pore volume, and average pore size of pure UiO-66, CdS and U6–CdS omposites with different weight contents of UiO-66.

Samples	S_{BET} (m^2/g)	Average pore size (nm)	Pore volume (cm^3/g)
CdS	57.05	11.72	0.063
20%U6–CdS	91.77	7.87	0.086
30%U6–CdS	155.09	8.31	0.188
40%U6–CdS	217.23	10.63	0.239
50%U6–CdS	407.63	8.72	0.243
60%U6–CdS	486.51	7.58	0.266
70%U6–CdS	638.46	8.97	0.290
UiO-66	1036.83	8.71	0.616

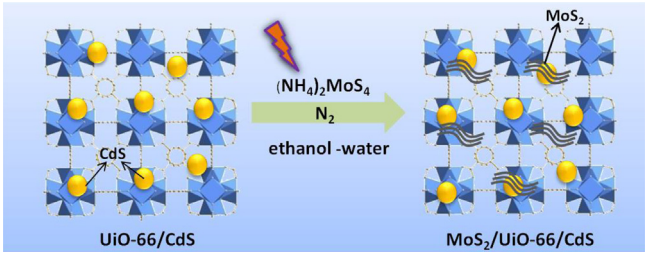

Fig. 3. Schematic chart for the fabrication of ternary MoS_2/UiO-66/CdS composites.

material). When CdS is coupled with UiO-66, type I adsorption–desorption isotherms are observed for the resulting U6–CdS composites. The BET surface area and pore volume for these samples are listed in Table 1. For the pure CdS and UiO-66, their BET surface areas are measured to be *ca.* 57 and 1036 m^2/g, respectively. In addition, it can be observed that the BET surface areas of U6–CdS composites get larger with the increase of UiO-66 content. It should be noted that the average pore sizes of the U6–CdS composites vary irregularly. This is mainly due to that the composites contain some voids generated by the random particle aggregation. Combining with the XRD and DRS results, it can be concluded that the current approach for preparation of U6–CdS is effective, which can preserve the structural property of the UiO-66. Moreover, it can be clearly seen that, the introduction of the UiO-66 greatly affect the properties of CdS.

Photodeposition (PD) technique has been employed to grow MoS_2 on U6–CdS using $(NH_4)_2MoS_4$ as a precursor. As schematically illustrated in Fig. 3, the as-synthesized U6–CdS composites are firstly dispersed in the mixed solution of ethanol and water and purged by nitrogen in a sealed vessel. After the light irradiation, MoS_2 nanosheets could be formed *in situ* on the surface of U6–CdS. This technique possesses two unique features: the synthetic strategy is simple and facile; the other is that the MoS_2 is directly deposited on the surface of UiO-66 without any surfactants, forming an intimate interfacial interaction between MoS_2 and U6–CdS, which would be beneficial for improving the interfacial electron transfer efficiency and enhancing the photocatalytic H_2 evolution activity [49].

The morphology and microscopic structure information of the samples are investigated by the SEM and TEM. As shown in Fig. 4a, the UiO-66 substrate displays some cubes nanocrystals and no significant change of the characteristic structure of UiO-66 is observed after CdS loading (Fig. 4b). The obtained CdS nanoparticles with average particle size in the range of 5–20 nm are well distributed on the surface of UiO-66 substrate without obvious aggregation. However, the pure CdS, prepared by the same hydrothermal method in the absence of UiO-66, is apt to aggregate to form CdS microspheres with a diameter of *ca.* 100 nm (Fig. 4c). TEM images of all the U6–CdS composites with different mass ratios of UiO-66 have also been shown to give a visual comparison (Fig. S2), which clearly shows that the sample with higher UiO-66 amount increases the dispersion of CdS and tends to form smaller CdS nanoparticles. The apparent contrast in the particle size of CdS is also in accordance with the DRS result, further demonstrating that the introduction of UiO-66 as support can effectively decrease the particle size and increase the dispersion of CdS nanoparticles. After the deposition of MoS_2, the morphology of the binary matrix still maintains, as displayed in Fig. 4d and e. But by comparing the TEM images of MoS_2/U6–CdS and U6–CdS, some fringes can be observed in the ternary MoS_2/U6–CdS composite. The wrinkles marked in Fig. 4e and f are the characteristic structure of the MoS_2 nanosheets. It is notable that some parts of the U6–CdS are even enwrapped by the MoS_2 showing strong interfacial contact (Fig. 4e and Fig. S3), and this is more obvious in the case of MoS_2/UiO-66 sample (Fig. 4g and Fig. S4). This intimate interaction among CdS, UiO-66 and MoS_2 components is believed would promote the fast transfer of photogenerated electrons from CdS to UiO-66 and MoS_2, thus enhancing the charge carriers separation and photocatalytic efficiency. The high resolution TEM (HRTEM) image of Fig. 4h shows clear fringes with lattice spacing of *ca.* 0.34 nm, which correspond to the (1 1 1) plane of hawleyite CdS [48]. The fringes of MoS_2 are hard to be observed due to the poor crystallinity aroused from the low synthesis temperature. In addition, the energy dispersive X-ray spectroscopy (EDX) analysis has also been carried out and the result is shown in Fig. 4i, which clearly demonstrates that the composite contains Zr, O, Cd, S and Mo elements. Moreover, it has been reported that such kind of MoS_2 is more efficient for catalytic H_2 evolution because it contains many active unsaturated sulfur atoms [52].

The chemical status of Cd, Mo and S in the representative MoS_2/U6–CdS composite is determined by X-ray photoelectron spectra (XPS) analysis. All the XPS peaks have been calibrated by the C 1s peak at 284.6 eV from the XPS instrument. As shown in Fig. 5a, the survey scan of the MoS_2/U6–CdS composite further confirms the existence of Zr, Cd, Mo, S, and O in the sample. No obvious peaks for impurity elements have been observed. For the Cd 3d spectrum in Fig. 5b, the spin orbit separation of Cd $3d_{5/2}$ is located at around 405.23 eV and the Cd $3d_{3/2}$ peak appears at 412.01 eV. The spin orbit separation of the 3d orbital is 6.78 eV, demonstrating that the Cd element in sample exists in the state of Cd^{2+} [53]. The high-resolution XPS spectrum in Fig. 5c shows the binding energies of the Mo $3d_{5/2}$ and Mo $3d_{3/2}$ peaks at 228.65 and 231.95 eV, respectively, which are typical values for Mo^{4+} in MoS_2 [54]. Fig. 5d displays the XPS spectrum of S 2p, which can be fitted into two peaks: S $2p_{3/2}$ and S $2p_{1/2}$, appearing at 161.45 and 163.1 eV, respectively, indicating the existence of S^{2-} [55]. The XPS results clearly prove the coexistence of MoS_2 and CdS in the MoS_2/U6–CdS composites.

3.2. Photocatalytic H_2 production

The photocatalytic H_2 production activity on MoS_2/U6–CdS composites has been evaluated in lactic acid aqueous solution under the irradiation of visible light ($\lambda \geq 420$ nm) together with that on Pt/U6–CdS for comparison. Control experiments indicate that no appreciable H_2 production has been detected in the absence of either light irradiation or photocatalyst, suggesting that H_2 production is driven by the photocatalytic process. As shown in Fig. 6, the photoactivity results indicate that the introduction of UiO-66 greatly affects the photocatalytic H_2 production activity of CdS, and it can also be observed that the content of UiO-66 in the composites has a significant influence on the photocatalytic activity. Taking a view of the overall activities, it can be seen that, with the addition of appropriate amount of UiO-66 in the composite, the activities of CdS for photocatalytic H_2 production have been significantly accelerated both in the case of using 1 wt% Pt or 1 wt% MoS_2 as cocatalysts. The optimum H_2 evolution can be obtained when the weight ratio of UiO-66 is 50%, reaching 515.4 μmol h^{-1} in the

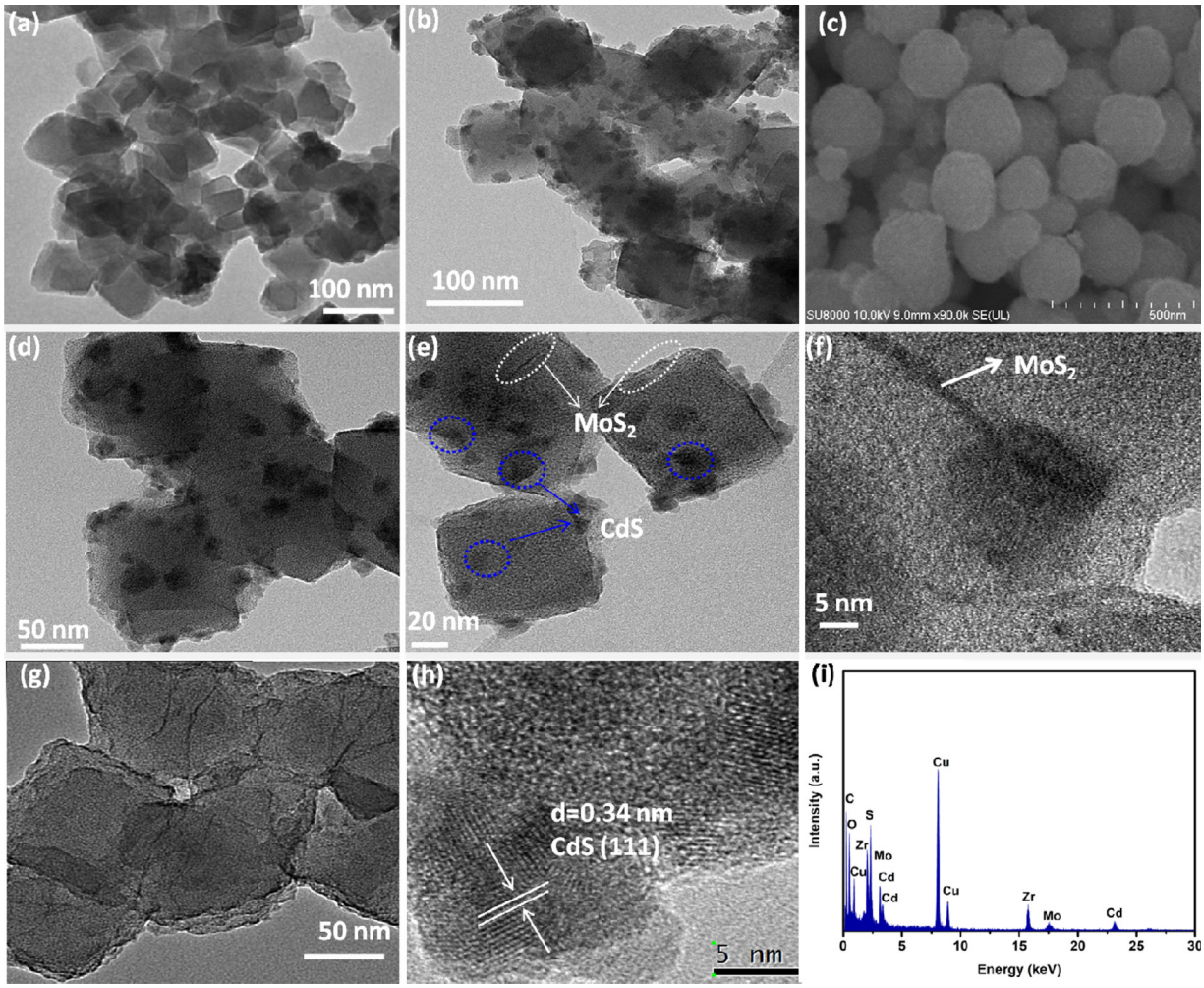

Fig. 4. TEM images of the pure UiO-66 (a) and 50% U6–CdS (b); SEM image of pure CdS (c); TEM images of 3% MoS_2/(50%) U6–CdS (d–f) and 3% MoS_2/UiO-66 (g); HRTEM image (h) and EDX image (i) of 3% MoS_2/(50%) U6–CdS.

presence of 1 wt% MoS_2. Notably, this photocatalytic H_2 evolution rate is not only significantly higher than the case of pure CdS, but also about 2-fold higher compared with that of 1 wt% Pt/U6–CdS under the same reaction conditions. These results suggest that the photodeposition of MoS_2 on the surface of U6–CdS is a very simple yet efficient approach for preparing high performance photocatalysts for H_2 evolution. Further increase the UiO-66 content in the MoS_2/U6–CdS composites leads to a deterioration of photocatalytic activity. This is understandable because accompanying with the increase of UiO-66, the content of the CdS, which is the only activity phase under the visible light irradiation, would be decreased relatively.

To study the effect of the MoS_2 content on the H_2 evolution rate, taking the optimal sample of 50% U6–CdS as substrate, a series of MoS_2/(50%) U6–CdS composites loaded with varying MoS_2 contents (0.5–3 wt%) have been prepared and investigated. As presented in Fig. 7, the rate of H_2 evolution on MoS_2/U6–CdS is increased with the increase of MoS_2 content initially, reaching a maximum H_2 evolution when the loading amount of MoS_2 in the composite is 1.5%. The H_2 production rate is up to 650 μmol h^{-1}. The apparent quantum efficiency (AQE) measured at an incident wavelength of 420 ± 10 nm over the 1.5% MoS_2/(50%) U6–CdS sample is *ca.* 23.6%. Further increase in the amount of MoS_2 leads to a gradual reduction of the photocatalytic activity. This probably results from the shading effect of MoS_2 [56,57], that is, the increased light absorption of MoS_2 caused by the higher content would impair the excitation of CdS. Because the MoS_2 co-catalyst is randomly deposited upon the surface of UiO-66 and CdS, for comparison, the photocatalytic H_2 production over MoS_2–CdS has also been investigated. Fig. S5 shows the variation in activity of CdS loaded with different amounts of MoS_2, a similar trend of the MoS_2 content on the activity can be observed. However, by comparison, it is obvious that the MoS_2/U6–CdS samples show much higher activity than MoS_2–CdS with the same content of MoS_2, clearly demonstrating the benefit of the UiO-66 in improving the photocatalytic H_2 evolution activity of CdS.

Stability is an important criterion to evaluate the performance of photocatalyst. As shown in Fig. 8, the XRD patterns of the fresh and used MoS_2/U6–CdS are almost the same, implying that the sample is stable during the photocatalytic reaction. Moreover, the MoS_2/U6–CdS shows considerable durability in four consecutive runs of totally 16 h, whereas the pure CdS displays significant loss in the photocatalytic activity (Fig. 9a). To describe clearly, the result of cycle run for the photocatalytic H_2 production over pure CdS is magnified and presented in Fig. 9b separately. The H_2 evolution amount over pure CdS has reduced by 50% after the four times recycling test. Furthermore, the ICP result demonstrates that the leaching of the Zr ion is so small that it can be ignored. And very

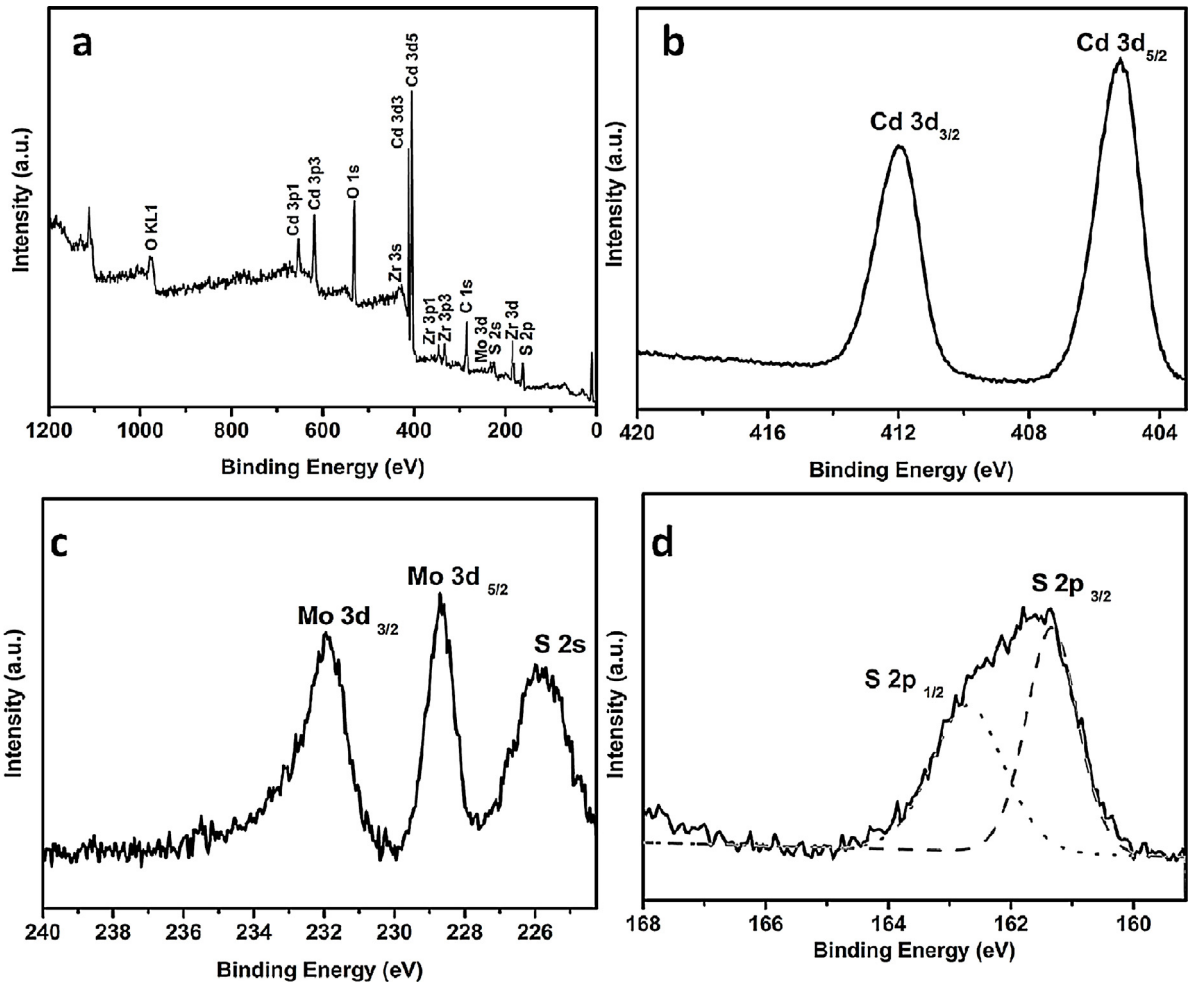

Fig. 5. XPS spectra of the 3% MoS_2/(50%) U6–CdS composite: survey spectrum (a), high resolution Cd 3d (b), Mo 3d (c) and S 2p (d) spectrum.

little Cd^{2+} (*ca.* 2.1%) of MoS_2/U6–CdS composites is leached out after photocatalytic process, while pure CdS nanoparticles are suffered from severe photocorrosion (*ca.* 30% Cd^{2+} leached out). This result implies that the synergetic effect between UiO-66 and MoS_2 cocatalyst can improve the photocatalytic H_2 evolution activity and anti-photocorrosion of CdS simultaneously.

3.3. Photoelectrochemical properties

To better understand the synergic action of UiO-66 and MoS_2 on enhancing the photocatalytic performance of CdS, the photocurrent test over the pure CdS, 50% U6–CdS and 1% MoS_2/(50%) U6–CdS has been performed. Fig. 10 shows a plot of photocurrent density transients for the three samples under the intermittent irradiation of visible light ($\lambda \geq 420$ nm). The fast photocurrent transient

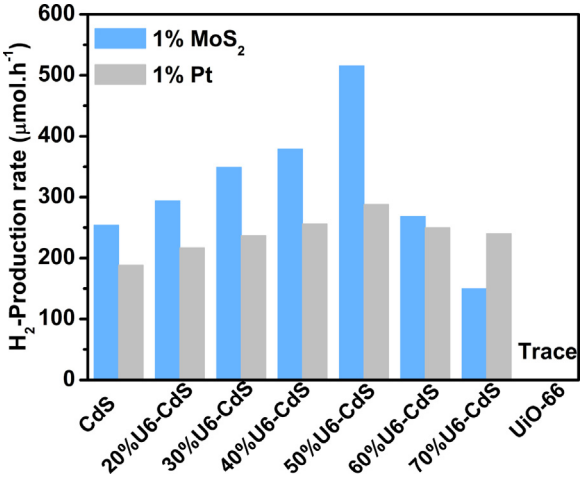

Fig. 6. The rate of H_2 production over pure CdS, UiO-66 and U6–CdS composites loaded with 1 wt% MoS_2 or Pt. Light source: 300 W Xe lamp, $\lambda \geq 420$ nm. Reaction solution: 80 mL of aqueous solution containing 10% of lactic acid in volume as a sacrificial agent. Catalyst: 20 mg.

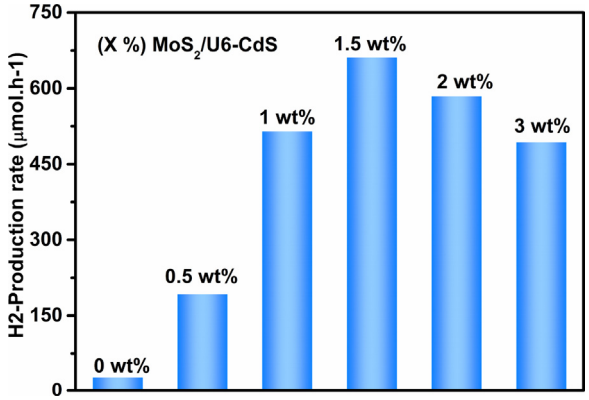

Fig. 7. The rate of H_2 production over 50% U6–CdS composite loaded with different amounts of MoS_2. Light source: 300 W Xe lamp, $\lambda \geq 420$ nm. Reaction solution: 80 mL of aqueous solution containing 10% of lactic acid in volume as a sacrificial agent. Catalyst: 20 mg.

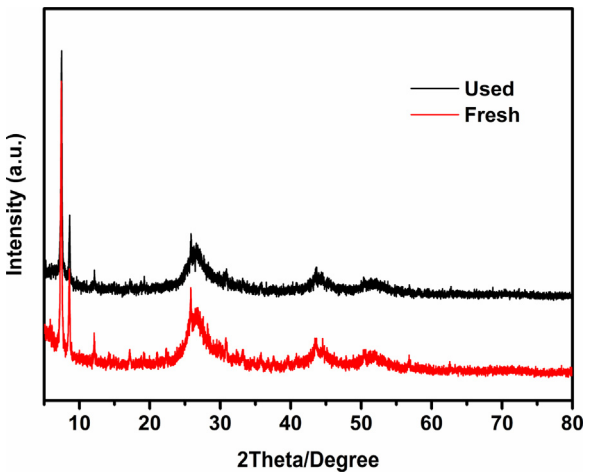

Fig. 8. XRD patterns of the 1% MoS_2/(50%) U6–CdS composites before and after the photocatalytic reaction.

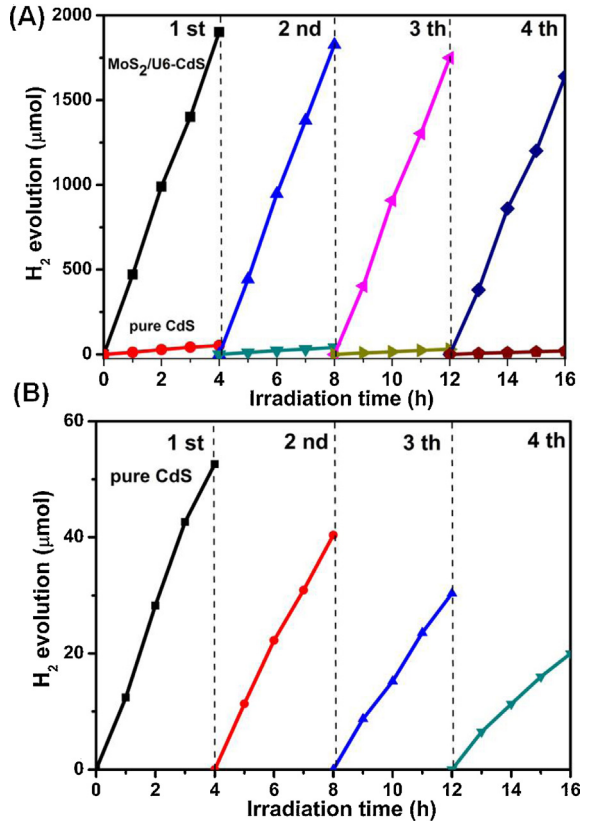

Fig. 9. Cycle runs for the photocatalytic H_2 production: (A) comparison between 1% MoS_2/(50%) U6–CdS and pure CdS; (B) magnified photostability result of pure CdS.

responses for switch-on and switch-off events have been observed over all the samples, underlining the photoactivated nature of the process. It is obvious that the 50% U6–CdS composite displays higher photocurrent transient response than pure CdS, suggesting that the introduction of UiO-66 as support for CdS improves the lifetime of photogenerated charge carriers. This is because that the LUMO of UiO-66 is estimated to be −0.60 V *vs.* NHE [58], which is less negative than the conduction band (CB) level of CdS (about −0.7 V *vs.* NHE) [59], therefore, the photogenerated electrons in the CB of CdS can transfer to UiO-66. The highest transient photocurrent is observed on the sample of 1% MoS_2/(50%) U6–CdS, indicating that the photodeposition of MoS_2 cocatalyst on the surface of (50%)

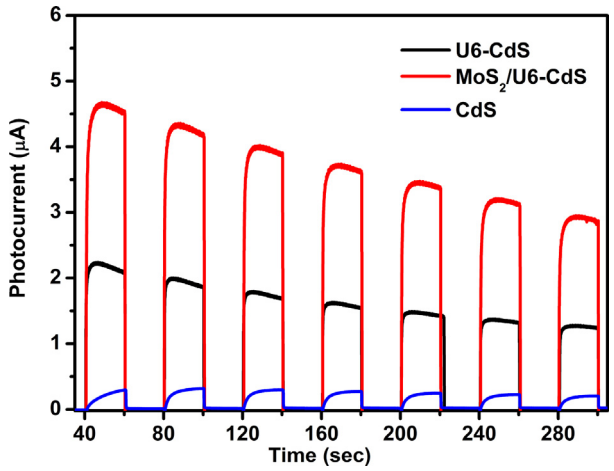

Fig. 10. Photocurrent spectra of the pure CdS, 50% U6–CdS and 1% MoS_2/(50%) U6–CdS under visible light irradiation ($\lambda \geq 420$ nm).

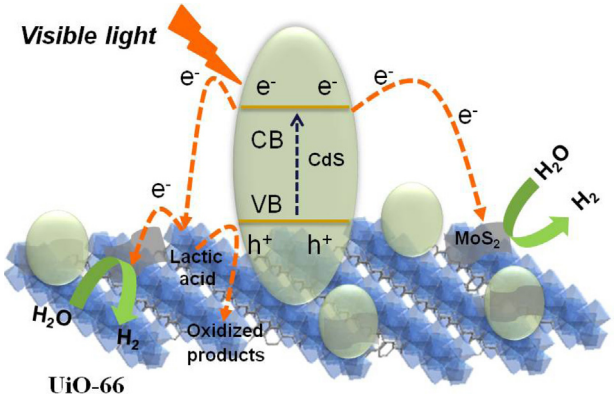

Fig. 11. Schematic illustration of the charge transfer in the MoS_2/U6–CdS composite under visible light irradiation ($\lambda \geq 420$ nm).

U6–CdS further suppresses the charge recombination, leaving more charge carriers to form reactive species which in turn results in the highest photocurrent response. This could be ascribed to the lowest CB level of MoS_2 (Fig. S6), favoring electrons transfer from the CB of CdS to MoS_2, and thus promotes the separation of charge carriers. The improved charge carrier separation and the prolonged lifetime of photogenerated electron–hole pairs can be further confirmed by the PL spectra. As displayed in Fig. S7, under excitation wavelength of 360 nm, for pure CdS, a broad band at 450–700 nm with a peak centered at approximately 550 nm is detected. The PL emission peak mainly arises from the recombination of excited electrons and holes and the intensity is a function of their concentrations [43,60,61]. By comparison, it can be found that the emission intensity of CdS is significantly decreased after the introduction of UiO-66 and MoS_2. The great attenuation in the PL intensity can be attributed to the lower recombination rate of electrons and holes in the presence of UiO-66 and particularly UiO-66/MoS_2. This also supports the rapid transfer of photogenerated electrons from CdS to UiO-66 and MoS_2.

3.4. Discussion of the photocatalytic mechanism

Based on the above discussion, a possible mechanism for the high H_2 production activity over MoS_2/U6–CdS sample has been proposed. As shown in Fig. 11, under visible light illumination, the electrons in the valence band (VB) of CdS are photoexcited to the conduction band (CB), creating holes in the VB. Due to the matched energy level of the LUMO of UiO-66 and CB level of CdS,

the photogenerated electrons in the CB of CdS can transfer to UiO-66. After the photodepositing of MoS_2 as cocatalyst, it can accept electrons and further improve the separation of the photogenerated electron–hole pairs [62,63]. Moreover, MoS_2 has been proved to act as active sites for H_2 evolution and the edges of the nanosized MoS_2 can promote the proton reduction for H_2 evolution [64]. Owing to the intimate interfacial contact among CdS, UiO-66 and MoS_2, the photogenerated electrons in the CB of CdS can transfer to MoS_2 nanosheets directly to react with the adsorbed H^+ ions at the edges of MoS_2 to produce H_2, or transfer to UiO-66 firstly and then to MoS_2 nanosheets to produce H_2. Meantime, the holes in the VB of CdS would be trapped by the sacrificial agent of lattice acid. The effective separation and consumption of the photoinduced electron–hole pairs, especially the holes, strongly enhance the photostability and restrain the photocorrosion of the CdS photocatalyst. Thus, the enhancement of the photocatalytic activity and photostability of CdS after UiO-66 introduction and MoS_2 modification can be attributed to the following factors: (1) UiO-66 has a large specific surface area which allows well dispersion of embedded CdS nanoparticles. This provides more adsorption sites and photocatalytic reaction centers that favor to improve the photocatalytic activity. Moreover, the large specific surface area of the composite is also beneficial for the adsorption and enrichment of holes sacrificial reagent on the surface of the photocatalyst, allowing for the effective capture of photogenerated holes. The rapid charge transfer and effective consumption of photogenerated holes by the sacrificial reagent would greatly restrain the oxidation of S^{2-} by holes in CdS, and then the photo-corrosion of CdS can be alleviated in the present system; (2) the separation of photogenerated charge carriers can be accelerated by forming the effective heterostructure between UiO-66 and CdS; (3) the photodeposition of MoS_2 cocatalyst on the surface of U6–CdS further improves the separation and transfer of the photogenerated electron–hole pairs and provide a large number of active sites to promote the H_2 evolution reaction. All these factors together contribute to the high activity and stability of the MoS_2/U6–CdS composites for the photocatalytic H_2 production.

4. Conclusions

In summary, we report a simple but highly cooperative ensemble with MoS_2 deposited on UiO-66 modified CdS. The MoS_2/U6–CdS composites formed with intimate spatial integration has remarkably hindered the aggregation of CdS nanoparticles, increased the surface area, reduced the recombination of photoexcited charge carriers and provided abundant reactive sites for H_2 evolution. As a result, they display as highly active noble-metal-free photocatalysts for H_2 production under visible light irradiation. More significantly, the obtained MoS_2/U6–CdS performs even better than Pt/U6–CdS under the same reaction conditions. This study clearly demonstrates the benefit of using MOFs as ideal support and MoS_2 as cocatalyst to work cooperatively for enhancing the photocatalytic H_2 evolution activity and stability of CdS. We anticipate that our proposed synthetic route will open up a new way for the fabrication of other highly efficient MOFs/MoS_2/semiconductor photocatalysts.

Acknowledgements

This work was supported by the National Natural Science Foundation of China (21273036 and 21177024) and National Key Basic Research Program of China (2014CB239303).

Appendix A. Supplementary data

Supplementary data associated with this article can be found, in the online version, at http://dx.doi.org/10.1016/j.apcatb.2014.11.056.

References

[1] M.-Q. Yang, N. Zhang, M. Pagliaro, Y.-J. Xu, Chem. Soc. Rev. (2014), http://dx.doi.org/10.1039/c4cs00213j.
[2] J. Zhang, J. Yu, M. Jaroniec, J.R. Gong, Nano Lett. 12 (2012) 4584–4589.
[3] R. Sasaki, K. Maeda, Y. Kako, K. Domen, Appl. Catal. B: Environ. 128 (2012) 72–76.
[4] J. Liu, S. Wen, Y. Hou, F. Zuo, G.J. Beran, P. Feng, Angew. Chem. Int. Ed. 52 (2013) 3241–3245.
[5] A. Gasparotto, D. Barreca, D. Bekermann, A. Devi, R.A. Fischer, P. Fornasiero, V. Gombac, O.I. Lebedev, C. Maccato, T. Montini, G. Van Tendeloo, E. Tondello, J. Am. Chem. Soc. 133 (2011) 19362–19365.
[6] Y.P. Xie, Z.B. Yu, G. Liu, X.L. Ma, H.-M. Cheng, Energy Environ. Sci. 7 (2014) 1895.
[7] P. Niu, L. Zhang, G. Liu, H.-M. Cheng, Adv. Funct. Mater. 22 (2012) 4763–4770.
[8] J. Hou, Z. Wang, W. Kan, S. Jiao, H. Zhu, R.V. Kumar, J. Mater. Chem. 22 (2012) 7291.
[9] Q. Xiang, B. Cheng, J. Yu, Appl. Catal. B: Environ. 138–139 (2013) 299–303.
[10] N. Zhang, Y. Zhang, X. Pan, X. Fu, S. Liu, Y.-J. Xu, J. Phys. Chem. C 115 (2011) 23501–23511.
[11] Q. Li, B. Guo, J. Yu, J. Ran, B. Zhang, H. Yan, J.R. Gong, J. Am. Chem. Soc. 133 (2011) 10878–10884.
[12] Y. Hu, X. Gao, L. Yu, Y. Wang, J. Ning, S. Xu, X.W. Lou, Angew. Chem. Int. Ed. 52 (2013) 5636–5639.
[13] Z. Fang, Y. Wang, J. Song, Y. Sun, J. Zhou, R. Xu, H. Duan, Nanoscale 5 (2013) 9830–9838.
[14] X. Chen, W. Chen, H. Gao, Y. Yang, W. Shangguan, Appl. Catal. B: Environ. 152–153 (2014) 68–72.
[15] Y. Shi, H. Li, L. Wang, W. Shen, H. Chen, ACS Appl. Mater. Interfaces 4 (2012) 4800–4806.
[16] J. Yu, J. Zhang, M. Jaroniec, Green Chem. 12 (2010) 1611–1614.
[17] A.M. Dennis, B.D. Mangum, A. Piryatinski, Y.S. Park, D.C. Hannah, J.L. Casson, D.J. Williams, R.D. Schaller, H. Htoon, J.A. Hollingsworth, Nano Lett. 12 (2012) 5545–5551.
[18] H. Yan, J. Yang, G. Ma, G. Wu, X. Zong, Z. Lei, J. Shi, C. Li, J. Catal. 266 (2009) 165–168.
[19] M.-Q. Yang, Y. Zhang, N. Zhang, Z.-R. Tang, Y.-J. Xu, Sci. Rep. 3 (2013) 3314–3320.
[20] S. Shen, L. Guo, Mater. Res. Bull. 43 (2008) 437–446.
[21] M.D. Hernandez Alonso, F. Fresno, S. Suarez, J.M. Coronado, Energy Environ. Sci. 2 (2009) 1231–1257.
[22] H.C. Zhou, J.R. Long, O.M. Yaghi, Chem. Rev. 112 (2012) 673–674.
[23] J. Lee, O.K. Farha, J. Roberts, K.A. Scheidt, S.T. Nguyen, J.T. Hupp, Chem. Soc. Rev. 38 (2009) 1450–1459.
[24] H. Furukawa, K.E. Cordova, M. O'Keeffe, O.M. Yaghi, Science 341 (2013) 1230444.
[25] R. Liang, L. Shen, F. Jing, W. Wu, N. Qin, R. Lin, L. Wu, Appl. Catal. B: Environ. 162 (2015) 245–251.
[26] T.K. Kim, K.J. Lee, J.Y. Cheon, J.H. Lee, S.H. Joo, H.R. Moon, J. Am. Chem. Soc. 135 (2013) 8940–8946.
[27] R. Peng, C.M. Wu, J. Baltrusaitis, N.M. Dimitrijevic, T. Rajh, R.T. Koodali, Chem. Commun. 49 (2013) 3221–3223.
[28] J. He, Z. Yan, J. Wang, J. Xie, L. Jiang, Y. Shi, F. Yuan, F. Yu, Y. Sun, Chem. Commun. 49 (2013) 6761–6763.
[29] L. Shen, S. Liang, W. Wu, R. Liang, L. Wu, J. Mater. Chem. A 1 (2013) 11473–11482.
[30] M. Alvaro, E. Carbonell, B. Ferrer, F.X. Llabres i Xamena, H. Garcia, Chemistry 13 (2007) 5106–5112.
[31] L. Shen, S. Liang, W. Wu, R. Liang, L. Wu, Dalton Trans. 42 (2013) 13649–13657.
[32] L. Ai, C. Zhang, L. Li, J. Jiang, Appl. Catal. B: Environ. 148–149 (2014) 191–200.
[33] Y. Horiuchi, T. Toyao, M. Saito, K. Mochizuki, M. Iwata, H. Higashimura, M. Anpo, M. Matsuoka, J. Phys. Chem. C 116 (2012) 20848–20853.
[34] J. Gao, J. Miao, P.-Z. Li, W.Y. Teng, L. Yang, Y. Zhao, B. Liu, Q. Zhang, Chem. Commun. 50 (2014) 3786–3788.
[35] L. Qi, J. Yu, M. Jaroniec, Phys. Chem. Chem. Phys. 13 (2011) 8915–8923.
[36] K. Maeda, T. Ohno, K. Domen, Chem. Sci. 2 (2011) 1362–1368.
[37] S. Fischer, D. Hollmann, S. Tschierlei, M. Karnahl, N. Rockstroh, E. Barsch, P. Schwarzbach, S.-P. Luo, H. Junge, M. Beller, S. Lochbrunner, R. Ludwig, A. Brückner, ACS Catal. 4 (2014) 1845–1849.
[38] M.A. Gross, A. Reynal, J.R. Durrant, E. Reisner, J. Am. Chem. Soc. 136 (2013) 356–366.
[39] T.F. Jaramillo, K.P. Jørgensen, J. Bonde, J.H. Nielsen, S. Horch, I. Chorkendor, Science 317 (2007) 100–102.
[40] Q. Xiang, J. Yu, M. Jaroniec, J. Am. Chem. Soc. 134 (2012) 6575–6578.
[41] X. Zong, H.J. Yan, G.P. Wu, G.J. Ma, F.Y. Wen, L. Wang, C. Li, J. Am. Chem. Soc. 130 (2008) 7176–7177.
[42] K. Chang, Z. Mei, T. Wang, Q. Kang, S. Ouyang, J. Ye, ACS Nano 8 (2014) 7078–7087.
[43] T. Jia, A. Kolpin, C. Ma, R.C.-T. Chan, W.-M. Kwok, S.C.E. Tsang, Chem. Commun. 50 (2014) 1185–1188.

[44] Z. Wang, J. Hou, C. Yang, S. Jiao, H. Zhu, Chem. Commun. 50 (2014) 1731–1734.
[45] Y. Li, H. Wang, S. Peng, J. Phys. Chem. C 118 (2014) 19842–19848.
[46] C. Gomes Silva, I. Luz, F.X. Llabres i Xamena, A. Corma, H. Garcia, Chemistry 16 (2010) 11133–11138.
[47] J.H. Cavka, S. Jakobsen, U. Olsbye, N. Guillou, C. Lamberti, S. Bor-diga, K.P. Lillerud, J. Am. Chem. Soc. 130 (2008) 13850–13851.
[48] N. Zhang, M.-Q. Yang, Z.-R. Tang, Y.-J. Xu, ACS Nano 8 (2014) 623–633.
[49] S. Kanda, T. Akita, M. Fujishima, H. Tada, J. Colloid Interface Sci. 354 (2011) 607–610.
[50] G.D. Stucky, J.E. Mac Dougail, Science 247 (1990) 669–678.
[51] H. Wu, Y.S. Chua, V. Krungleviciute, M. Tyagi, P. Chen, T. Yildirim, W. Zhou, J. Am. Chem. Soc. 135 (2013) 10525–10532.
[52] J. Xie, H. Zhang, S. Li, R. Wang, X. Sun, M. Zhou, J. Zhou, X.W. Lou, Y. Xie, Adv. Mater. 25 (2013) 5807–5813.
[53] L. Ge, F. Zuo, J. Liu, Q. Ma, C. Wang, D. Sun, L. Bartels, P. Feng, J. Phys. Chem. C 116 (2012) 13708–13714.
[54] X. Zong, Z. Xing, H. Yu, Y. Bai, G.Q. Lu, L. Wang, J. Catal. 310 (2014) 51–56.
[55] Y. Huang, Y. Chen, C. Hu, B. Zhang, T. Shen, X. Chen, M.Q. Zhang, J. Mater. Chem. 22 (2012) 10999–11002.
[56] C. Liu, L. Wang, Y. Tang, S. Luo, Y. Liu, S. Zhang, Y. Zeng, Y. Xu, Appl. Catal. B: Environ. 164 (2015) 1–9.
[57] Y. Hou, A.B. Laursen, J. Zhang, G. Zhang, Y. Zhu, X. Wang, S. Dahl, I. Chorkendorff, Angew. Chem. Int. Ed. 52 (2013) 3621–3625.
[58] R. Lin, L. Shen, Z. Ren, W. Wu, Y. Tan, H. Fu, J. Zhang, L. Wu, Chem. Commun. 50 (2014) 8533–8535.
[59] J. Ran, J. Yu, M. Jaroniec, Green Chem. 13 (2011) 2708–2713.
[60] Y. Zhang, Z. Chen, S. Liu, Y.-J. Xu, Appl. Catal. B: Environ. 140–141 (2013) 598–607.
[61] M.-Q. Yang, B. Weng, Y.-J. Xu, Langmuir 29 (2013) 10549–10558.
[62] G. Chen, N. Ding, F. Li, Y. Fan, Y. Luo, D. Li, Q. Meng, Appl. Catal. B: Environ. 160–161 (2014) 614–620.
[63] W. Zhou, Z. Yin, Y. Du, X. Huang, Z. Zeng, Z. Fan, H. Liu, J. Wang, H. Zhang, Small 9 (2013) 140–147.
[64] Y.D. Hou, B.L. Abrams, P.C.K. Vesborg, M.E. Bjorketun, K. Herbst, L. Bech, A.M. Setti, C.D. Damsgaard, T. Pedersen, O. Hansen, J. Rossmeisl, S. Dahl, J.K. Nørskov, I. Chorkendor, Nat. Mater. 10 (2011) 434–438.